Research Article | Vol. 29, No. 10 / 10 May 2021 / Optics Express 15830
Optics EXPRESS

Excitation of nonlinear beams: from the linear Talbot effect through modulation instability to Akhmediev breathers

ROLAND SCHIEK*

Ostbayerische Technische Hochschule Regensburg, Prüfeninger Straße 58, 93049 Regensburg, Germany
*roland.schiek@oth-regensburg.de

Abstract: The smooth transition between stable, Talbot-effect-dominated and modulationally unstable nonlinear optical beam propagation is described as the superposition of oscillating, growing and decaying eigenmodes of the common linearized theory of modulation instability. The saturation of the instability in form of breather maxima is embedded between eigenmode growth and decay. This explains well the changes of beam characteristics when the input intensity increases in experiments on modulation instability and breather excitation in spatial-spatial experimental platforms. An increased accuracy of instability gain measurements, a variety of interesting nonlinear beam scenarios and a more selective and well-directed breather excitation are demonstrated experimentally.

© 2021 Optical Society of America under the terms of the OSA Open Access Publishing Agreement

1. Introduction

Pulse propagation in optical fibers and one-dimensional (1D) beam propagation, for example in an optical slab waveguide, are theoretically described by the nonlinear Schrödinger equation (NLSE)

$$\frac{\partial u}{\partial z} - i\beta_2 \frac{\partial^2 u}{\partial x^2} = -i\gamma |u|^2 u. \tag{1}$$

z is the propagation distance along the fiber or the waveguide. For pulse propagation x is the time and for beam propagation x is the transverse coordinate across the beam. β_2 stands for dispersion or diffraction. $|u|^2$ is proportional to the pulse envelope or the beam shape and γ is the nonlinearity. Note that we use a form of the NLSE that is consistent with our notation in the last 35 years and which is standard in electrical engineering with the Ansatz $e^{i(\omega t - \beta z)}$ [1]. The more familiar notation in physics is obtained by the conjugate complex of the expressions. A stable continuous wave (cw) solution of Eq. (1) at low intensity becomes unstable above a certain intensity level. The instability is well understood and investigated in the theory of modulation instability (MI) where the evolution of a small additive sinusoidal modulation on the cw solution is described in a linearized approximation [2,3]. In optical systems noise generated MI was observed as beam breakup from the early days of nonlinear optics. The first temporal modulation-initiated MI experiments demonstrated the generation of — at the time not easy to produce — trains of short pulses with high repetition rates from weakly modulated cw input [4]. MI gain measurements were performed also with small modulation injection [5].

Shortly after the theory of MI, exact analytical solutions extending and containing the MI scenario were reported [6]. For experimental investigations two doubly periodic breather families [6,7], the Akhmediev breather with infinite period as separatrix between them, and modifications of these solutions like moving breathers (with nonzero velocity) [8] and higher-order breathers [9] became the most important. During the last ten years seeded temporal breathers in pulses on optical fibers [10–12] and in deep water waves [7,13] were excited. MI-induced formation of arrays of spatial solitons in a planar waveguide was the first observation of the growing part of a

#425626 https://doi.org/10.1364/OE.425626
Journal © 2021 Received 22 Mar 2021; revised 27 Apr 2021; accepted 29 Apr 2021; published 7 May 2021

Optics EXPRESS

spatial breather [14]. The first complete cycles of breathers in nonlinear beam propagation have been reported very recently [15,16].

The importance of the correct initial conditions was recognized. While in the first experiments any convenient modulation was used [4,5,10,11], later the importance of the actual phase of the modulation was considered. The dynamic evolution of the two breather families, selectively launched by phase adjustment, has been characterized in very good detail and agreement to theory [12,17]. With special modulation schemes and phase control it was also possible to excite more sophisticated breathers like higher-order breathers [18] and moving breathers for investigation of breather interactions [19–21].

In a water tank it is straightforward to observe the evolution of breather dynamics with amplitude and phase along the propagation direction. In optics the output after different fiber lengths provides information on the dynamics along the propagation distance [21–23]. In the newest fiber optics experiments [12,17] the dynamics along the propagation became also accessible by use of a kind of optical time domain reflectometer. It could be summarized that fiber optics and water tank experiments demonstrated the most important characteristics of breathers pretty well and completely. The first comprehensive summaries are found already in textbooks [24].

This is different yet for the still very new platforms for breathers in spatial nonlinear beam propagation. Till now it is not possible to observe the breather dynamics directly inside the propagation medium without cutting back the sample, as done in older fiber experiments [11]. In bulk this may not change, in waveguides or nematic crystals there is the option to observe the evolution from the top of the sample [25]. However, a powerful alternative to characterize nonlinear beam propagation without cutting back the sample is the observation of the output beam dependent on input intensity. First used in older fiber experiments [10,26], the composition of the output in normalized intensity scans was the presentation form of the first spatial breathers [15,16]. These intensity-scan figures do not exactly show the dynamics of one specific breather or MI scenario because some parameters change with intensity. On the other hand they document all facets of MI and, beyond the limits of MI, the breather regime by showing the whole intensity-dependent characteristics of nonlinear beam propagation in one picture. In the — so far not much highlighted — low-intensity end of the intensity scans linear and weakly-nonlinear beam propagation is shown as well as the transition from weakly- to strongly-nonlinear waves at the other end. Figure 1 shows two examples of measured intensity scans with completely different low- and medium-intensity scenarios and the transition through MI to highly-nonlinear breather beams. While Fig. 1(a) resembles monotone growing modulation as expected from MI, the decay of the modulation with increasing input intensity in Fig. 1(b) indicates a more curious behavior.

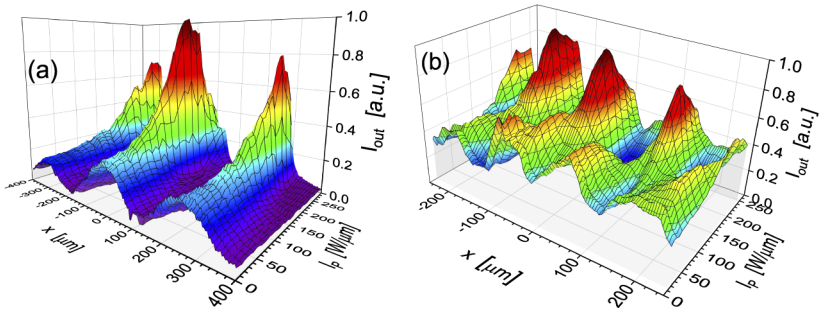

Fig. 1. Normalized output intensity distribution $I_{\mathrm{out}}(x)$ dependent on the peak input intensity I_{P}: (a) modulation period 300 μm and contrast 0.24, $\gamma = 0.35 \times 10^{-6}\ \frac{1}{\mathrm{m}}$; (b) modulation period 133 μm and contrast 0.11, $\gamma = 0.58 \times 10^{-6}\ \frac{1}{\mathrm{m}}$. Parameters are explained in the text.

Optics EXPRESS

In this article we explain the details of this intensity-dependent beam transformation and the influence of the input on MI and the evolving breathers. The work was initiated by our experiments on breathers in nonlinear beam propagation in slab waveguides. It summarizes those characteristics of breathers that we found important for performing and interpreting breather experiments. As a result, an increased accuracy of instability gain measurements and a more selective and well-directed breather excitation could be demonstrated experimentally.

2. Nonlinear beams, theoretical reminiscence

In order to investigate MI and breathers experimentally it is advantageous to seed the cw solution $u(z) = \sqrt{P}e^{-i\gamma P z}$ of Eq. (1) at the input $z = 0$ with a weak modulation $\varepsilon(x)$. The unit-less P times a unit intensity $p_0 = 1\ \frac{\mathrm{W}}{\mathrm{m}}$ of a normalized slab waveguide mode is the intensity of the unmodulated 1D beam. The most general sinusoidal modulation is

$$\varepsilon(x) = \varepsilon_\mathrm{s} e^{-i\omega_\mathrm{m} x} + \varepsilon_\mathrm{a} e^{i\omega_\mathrm{m} x}. \tag{2}$$

For small modulation amplitudes the modulation can be considered a perturbation of the cw solution $u(x,z) = (\sqrt{P} + \varepsilon(x,z))e^{-i\gamma P z}$. The well known linearization from MI theory yields a linear differential equation system for the evolution of the two perturbation contributions $\varepsilon_\mathrm{s}(z)$ and $\varepsilon_\mathrm{a}(z)$. The two eigenvalues

$$\lambda_\mathrm{A,B} = \pm\sqrt{\beta_2^2\omega_\mathrm{m}^4 - 2|\beta_2|\omega_\mathrm{m}^2\gamma P} \tag{3}$$

with the corresponding eigenvectors

$$\begin{pmatrix} e_\mathrm{1A,B} \\ e_\mathrm{2A,B} \end{pmatrix} = \begin{pmatrix} 1 \\ \frac{-\beta_2\omega_\mathrm{m}^2 - \gamma P + \lambda_\mathrm{A/B}}{\gamma P} \end{pmatrix} \tag{4}$$

determine the evolution of the perturbation in z direction

$$\begin{pmatrix} \varepsilon_\mathrm{s}(z) \\ \varepsilon_\mathrm{a}^*(z) \end{pmatrix} = A \begin{pmatrix} e_\mathrm{1A} \\ e_\mathrm{2A} \end{pmatrix} e^{-i\lambda_\mathrm{A} z} + B \begin{pmatrix} e_\mathrm{1B} \\ e_\mathrm{2B} \end{pmatrix} e^{-i\lambda_\mathrm{B} z}. \tag{5}$$

Note that there are always two eigenvectors that are equally important, even though in the MI literature mostly only the growing one is considered. With the perturbation evolution Eq. (5) and the eigenvectors in Eq. (4) the input modulation evolves in z direction as

$$\begin{aligned} \varepsilon(x,z) = &\left[Ae^{-i\lambda_\mathrm{A} z} + Be^{-i\lambda_\mathrm{B} z}\right] e^{-i\omega_\mathrm{m} x} + \\ &+ \left[A\frac{-\beta_2\omega_\mathrm{m}^2 - \gamma P + \lambda_\mathrm{A}}{\gamma P} e^{-i\lambda_\mathrm{A} z} + B\frac{-\beta_2\omega_\mathrm{m}^2 - \gamma P + \lambda_\mathrm{B}}{\gamma P} e^{-i\lambda_\mathrm{B} z}\right]^* e^{i\omega_\mathrm{m} x}. \end{aligned} \tag{6}$$

For beam description the diffraction term $\beta_2 = -\frac{1}{2k_\mathrm{wv}}$ is always negative and proportional to the inverse of the wavevector $k_\mathrm{wv} = \frac{2\pi n}{\lambda_0}$ with the vacuum wavelength λ_0 and refractive index n. The spatial modulation frequency $\omega_\mathrm{m} = \frac{2\pi}{X}$ is given by the modulation period X.

2.1. Talbot effect and weakly-nonlinear beams

For small intensity-nonlinearity products $2\gamma P < |\beta_2|\omega_\mathrm{m}^2$ the eigenvalues in Eq. (3) are real numbers and the modulation-induced perturbation oscillates along z. The system is stable and the beam pattern resembles the linear Talbot effect with a simple nonlinear modification of the periodicity. A few examples of beam intensities calculated with Eq. (6) from the perturbation theory are

Optics EXPRESS

shown in Fig. 2. The used parameters yield beam patterns similar to what we discuss later in the experimental section. Figure 2(a) shows a typical linear Talbot effect pattern with a symmetric two-sideband input modulation $\varepsilon_s = \varepsilon_a = \frac{\eta}{2}e^{i\varphi}$. Experimentally this corresponds to a pump propagation along z plus two symmetrically against the z axis tilted beams with equal and weaker amplitudes, as it was implemented in [15]. From the input modulation $\varepsilon(x, z = 0) = \eta e^{i\varphi}\cos(\omega_m x)$ the integration constants in Eq. (5) $A = \frac{\eta}{4\lambda_A}[e^{-i\varphi}\gamma P + e^{i\varphi}(\beta_2\omega_m^2 + \gamma P + \lambda_A)]$ and $B = \frac{\eta}{2}e^{i\varphi} - A$ are calculated and Eq. (6) reduces to the simpler form

$$\varepsilon(x, z) = (Ae^{-i\lambda_A z} + Be^{i\lambda_A z})2\cos(\omega_m x). \tag{7}$$

The periodicity $Z = \frac{2\pi}{\lambda_A}$ of the Talbot pattern in propagation direction is given by the power-dependent eigenvalue λ_A in Eq. (3). The smallest periodicity $Z_T = \frac{2\pi}{|\beta_2|\omega_m^2}$ (Talbot periodicity) is obtained for a negligible intensity-nonlinearity product. With the phase φ the input modulation is changed from pure amplitude modulation ($\varphi = 0$ and π) to approximate frequency modulation ($\varphi = \pm\frac{\pi}{2}$). A phase variation shifts the pattern in z direction and the maximum modulation amplitude changes. In Fig. 2(b) we observe the nonlinear modification of the Talbot effect. The pattern periodicity Z increases with decreasing λ_A for growing nonlinearity. This behavior continues till for $2\gamma P = |\beta_2|\omega_m^2$ the eigenvalue becomes zero and Z becomes infinite, i.e. the input modulation does not change at all as shown in Fig. 2(c). However, the effect is cleanly observed for small phases φ only when Eq. (7) in the limiting form $\eta\cos(\lambda_A z)\cos(\omega_m x)$ represents a cosine in z with infinity period and maximum at $z = 0$. For $\varphi \neq 0$ and P approaching $P_c = \frac{|\beta_2|\omega_m^2}{2\gamma}$ the coefficient A is approximated by $A = -i\frac{\eta\gamma P\sin\varphi}{2\lambda_A}$ with a growing absolute value $|A|$ and $B \Rightarrow A^*$. Therefore, the modulation evolution in Eq. (7) simplifies to

$$\varepsilon(x, z) = \mp 4|A|\sin(\lambda_A z)\cos(\omega_m x) = -\frac{2\eta\gamma P\sin\varphi}{\lambda_A}\sin(\lambda_A z)\cos(\omega_m x), \tag{8}$$

with period Z and amplitude $4|A|$ going to infinity, now with a completely different behavior. At the input close to the zero of the sine the modulation grows linearly for small $z << Z$. This applies (for real ε) also to the modulation of the intensity $|\sqrt{P} + \varepsilon|^2 \approx P + 2\sqrt{P}\varepsilon$ which is also proportional to ε as long as $\varepsilon^2 << 2\sqrt{P}|\varepsilon|$. As an example, Fig. 2(d) shows the strong difference to Fig. 2(c) when the phase φ is changed from 0 to $\frac{\pi}{4}$, with otherwise same parameters. The phase φ determines a fine shift of the zero of the sine close to $z = 0$ and influences the modulation amplitude with the factor $\sin\varphi$. However, for a correct reproduction of the region close to $z = 0$ the approximation Eq. (8) is too rough.

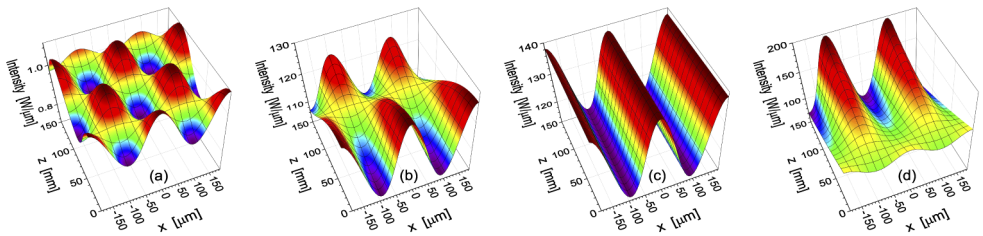

Fig. 2. Evolution of a symmetric two-sideband x-modulated input intensity along the propagation direction: (a) Talbot effect, negligible nonlinearity $\gamma P = 0.217\,\frac{1}{m}$, $\varphi = 0$; (b) $\gamma P = 25.0\,\frac{1}{m}$, $\varphi = 0$; (c) $\gamma P = 27.25\,\frac{1}{m} \lessapprox \gamma P_c$, $\varphi = 0$; (d) $\gamma P = 27.25\,\frac{1}{m}$, $\varphi = \frac{\pi}{4}$. Parameters similar to our experimental conditions $\beta_2 = -47.265\times10^{-9}$ m and $\omega_m = \frac{2\pi}{185\,\mu m}$.

Figure 3 shows not so typical Talbot effect patterns with a one-sideband input modulation $\varepsilon(x, z = 0) = \eta e^{i\varphi}e^{i\omega_m x}$. Experimentally this corresponds to a pump propagating along z plus

Optics EXPRESS

one weaker beam that is tilted against the z axis, as it was used for MI measurements in [5] and breather excitations in [16]. The phase φ introduces now only a transverse shift along x and is set to $\varphi = 0$ without loss of generality. With the integration constants $A = \frac{\eta\gamma P}{2\lambda_A}$ and $B = -A$ Eq. (6) reduces for the one-sideband modulation and for a negligible intensity-nonlinearity product to

$$\varepsilon(x, z) = \eta e^{i(\omega_m x + |\beta_2|\omega_m^2 z)}. \tag{9}$$

The input modulation is shifted increasingly to the left with increasing z. The disturbance in Eq. (9) creates the interference fringe pattern of two tilted plane waves as shown in Fig. 3(a). The angle between the propagating fringe pattern and the z axis is $\arctan(|\beta_2|\omega_m)$ which is half the tilt angle of the weak modulation beam. After each Talbot periodicity the input pattern repeats. Figures 3(b) and (c) show the nonlinear modification of the tilted fringe pattern for larger intensity. The eigenvalue λ_A decreases, the recurrence periodicity $Z = \frac{2\pi}{\lambda_A}$ increases. After a short distance of adjusting and locking the position of the fringes, self-focused structures develop which propagate more parallel to the z axis. Further on, the self-focused structures decay and the fringe pattern starts moving again till the next not-moving self-focused structure develops. Because the self-focused fringe portions propagate parallel to the z-axis, the whole fringe pattern moves step-like with an average shift rate corresponding to the nonlinearly increased periodicity Z. When the intensity approaches $P_c = \frac{|\beta_2|\omega_m^2}{2\gamma}$, Eq. (6) takes the form

$$\varepsilon(x, z) = \eta \cos(\lambda_A z) e^{i\omega_m x} - \frac{2\eta\gamma P}{\lambda_A} \sin(\lambda_A z) \sin(\omega_m x). \tag{10}$$

For growing z the first term can be neglected and the dominant second term describes exactly the same field evolution that we found in Eq. (8) for $\varphi = \frac{\pi}{2}$. A shift of the fringe pattern by a quarter of the period X is the only important modification. The $\cos(\omega_m x)$ in Eq. (8) is replaced by $\sin(\omega_m x)$ in Eq. (10). The similarity between one- and two-sideband modulation can be seen from the comparison of Fig. 3(d) and Fig. 2(d). Only for small z the interference between comparably strong terms in Eq. (10) causes a difference. Except in this region of a fringe movement the beams in both figures show increasingly similar characteristics for growing z. While the scaling factor $\sin\varphi$ in Eq. (8) introduces for the two-sideband modulation a phase-dependent strength of the modulation pattern, the one-sideband excitation has the advantage of being phase insensitive with always maximum strength. The equal final field evolution from one- and two-sideband modulation is also explained by four-wave mixing that generates the missing sideband in the early propagation stage (see also section 4.3 and [27]).

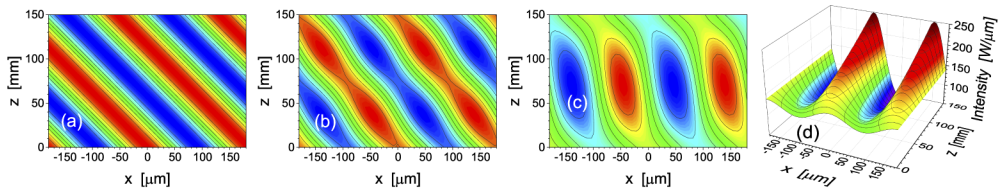

Fig. 3. Evolution of a one-sideband x-modulated input intensity along the propagation direction: (a) Talbot effect, negligible nonlinearity $\gamma P = 0.217\,\frac{1}{m}$; (b) $\gamma P = 10.9\,\frac{1}{m}$; (c) $\gamma P = 22.8\,\frac{1}{m}$; (d) $\gamma P = 27.25\,\frac{1}{m} \lessapprox \gamma P_c$. Diffraction and periodicity as in Fig. 2, calculation based on Eq. (6).

The solutions of the perturbation theory are restricted to small modulation amplitudes compared to the background $\eta << \sqrt{P}$ where the linearization is valid. Figure 4 compares our analytical solutions with numerical simulations. Very good agreement is found for normalized input field modulation amplitudes $\frac{\eta}{\sqrt{P}} < 5\,\%$ (corresponding approximately to intensity modulation

Optics EXPRESS

amplitudes $\frac{2\sqrt{P}\eta}{P}$<10 %) as long as the modulation does not grow too big and does not saturate. However, even in the case of an intensity modulation growing up to ≈ ±50 % in Fig. 4(c) the accuracy is reasonably good.

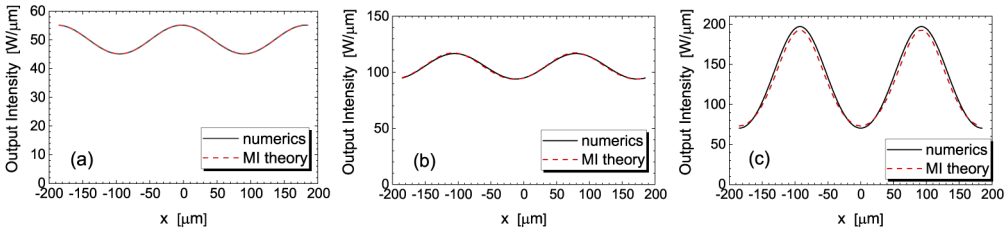

Fig. 4. Comparison of the output intensity calculated with simulation and linearized MI theory: (a) data from Fig. 3(b); (b) data from Fig. 3(c); (c) data from Fig. 2(d).

It is worth to note that only nonlinear modifications of the linear Talbot effect can be observed under stable and weakly-nonlinear conditions. The "Nonlinear Talbot Effect" on the other hand is an interpretation of doubly periodic solutions of the NLSE in the unstable highly nonlinear regime [28].

2.2. Modulation instability

For intensity-nonlinearity products above a threshold $2\gamma P>|\beta_2|\omega_\mathrm{m}^2$ the eigenvalues in Eq. (3) become pure imaginary numbers $\lambda_{\mathrm{A,B}} = \pm ig$ with the gain factor $g = \sqrt{2|\beta_2|\omega_\mathrm{m}^2\gamma P - \beta_2^2\omega_\mathrm{m}^4}$.

The eigenvectors from Eq. (4) describe a modulation-induced perturbation with pure exponential growth or decay. The system is now unstable. Equation (6) simplifies with the imaginary eigenvalues to

$$\begin{aligned}\varepsilon(x,z) = &\left[Ae^{gz} + Be^{-gz}\right]e^{-i\omega_\mathrm{m}x} + \\ &+ \left[A^*e^{i\psi}e^{gz} + B^*e^{-i\psi}e^{-gz}\right]e^{i\omega_\mathrm{m}x}\end{aligned} \tag{11}$$

with $\psi = \arctan\frac{-g}{|\beta_2|\omega_\mathrm{m}^2-\gamma P}$ for positive $|\beta_2|\omega_\mathrm{m}^2 - \gamma P$ and $\psi = \arctan\frac{-g}{|\beta_2|\omega_\mathrm{m}^2-\gamma P} - \pi$ for negative $|\beta_2|\omega_\mathrm{m}^2 - \gamma P$. Note that ψ is in our notation always a negative angle. Equation (11) can be separated in a growing and decaying part

$$\begin{aligned}&\varepsilon(x,z) = \varepsilon^+ + \varepsilon^- = \\ &2|A|e^{i\frac{\psi}{2}}\cos(\omega_\mathrm{m}x + \frac{\psi}{2} - \alpha_\mathrm{A})e^{gz} + 2|B|e^{-i\frac{\psi}{2}}\cos(\omega_\mathrm{m}x - \frac{\psi}{2} - \beta_\mathrm{B})e^{-gz}.\end{aligned} \tag{12}$$

α_A and β_B are the phases of A and B. For a symmetric two-sideband input modulation $\varepsilon(x, z = 0) = \eta e^{i\varphi}\cos(\omega_\mathrm{m}x)$ the integration constants are $A = \frac{\eta}{2}e^{i\frac{\psi}{2}}\frac{\sin(\frac{\psi}{2}+\varphi)}{\sin\psi}$ and $B = \frac{\eta}{2}e^{-i\frac{\psi}{2}}\frac{\sin(\frac{\psi}{2}-\varphi)}{\sin\psi}$. Only for an input phase $\varphi = \pm\frac{\psi}{2}$ a pure growing or decaying MI solution is excited, respectively. The growing MI solution has the form

$$\varepsilon^+_{\mathrm{2SB}}(x,z) = \eta e^{i\frac{\psi}{2}}\cos(\omega_\mathrm{m}x)e^{gz}. \tag{13}$$

For experimental measurements of MI gain with two-sideband modulation the modulation phase is critical and needs to be controlled. However, the decaying solution may be neglected compared to the growing solution for larger propagation lengths. A careful consideration of the characteristic length $\tau = \frac{1}{g}$, the sample length and especially the ratio $|A/B|$ is crucial for determining the gain in a not phase-controlled experiment. Figure 5 compares growing, decaying and mixed MI solutions for different input phases φ.

Optics EXPRESS

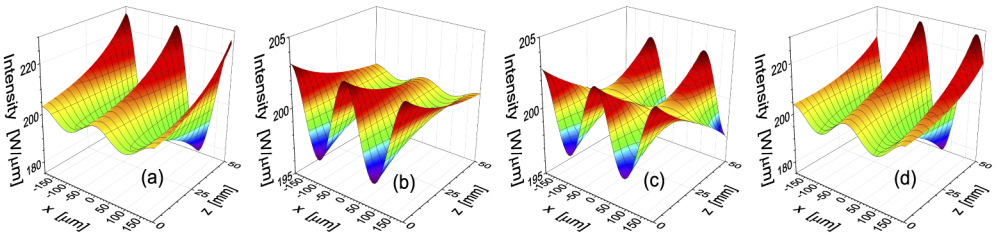

Fig. 5. MI wave propagation: (a) growing eigenmode, two-sideband excitation with $\varphi = -37.54°$; (b) decaying eigenmode, two-sideband excitation with $\varphi = 37.54°$; (c) growing and decaying MI, two-sideband excitation with $\varphi = 45°$; (d) one-sideband excitation. Diffraction and periodicity as in Fig. 2, $\gamma P = 43.4\,\frac{1}{\mathrm{m}}$, eigenmode angle $\frac{\psi}{2} = -37.54°$.

From an experimental point of view the one-sideband modulation $\varepsilon(x, z = 0) = \eta e^{i\omega_m x}$ has the automatic advantage of equal growing and decaying solution parts with $A = \frac{i\eta}{2\sin\psi}$ and $B = -A$ having the same absolute value. When the decaying solution can be neglected against the growing solution for $z>\tau$, the evolving modulation

$$\varepsilon^{+}_{1SB}(x, z) = \frac{\eta}{|\sin\psi|} e^{i\frac{\psi}{2}} \cos(\omega_m x + \frac{\psi}{2} + \frac{\pi}{2}) e^{gz} = -\frac{\eta}{|\sin\psi|} e^{i\frac{\psi}{2}} \sin(\omega_m x + \frac{\psi}{2}) e^{gz} \tag{14}$$

is very similar to the pure growing eigenmode in Eq. (13). The factor $\frac{1}{\sin\psi}$ can be corrected easily and a phase-insensitive excitation of a growing eigenmode is possible in a one-sideband modulation scheme. Figure 5(d) compares a one-sideband-generated growing eigenmode with the pure growing eigenmode in Fig. 5(a).

Again the solutions are restricted to small modulation amplitudes compared to the background $\eta << \sqrt{P}$ where the linearization is valid. Because of the growing eigenmode the validity of the linearized MI solutions is restricted to a limited propagation regime. In the examples in Fig. 5 the deviation between the linearized MI theory and a numerical simulation is less than one percent.

2.3. Breathers

When the unstable MI solution saturates and the linearized perturbation theory does no longer apply, breather solutions of the NLSE describe pulse and beam propagation [29]. After growing MI, the focusing saturates in highly localized intensity peaks which relax in decaying MI after the localization. This process repeats periodically and forms a breather. We restrict our discussion to a parameter range where only one modulation frequency is modulationally unstable (no higher-order breathers). Figure 6 shows the — in our context — important breathers. The best known, and a kind of basic unit of these solutions, is the Akhmediev breather (AB) [6]

$$u(x, z) = i\sqrt{P} e^{-iz'} \left[\frac{(1 - 4a)\cosh(bz') - ib\sinh(bz') + \sqrt{2a}\cos(\omega_m x)}{\sqrt{2a}\cos(\omega_m x) - \cosh(bz')} \right] \tag{15}$$

with the constants $a = \frac{1}{2}(1 - (\frac{\omega_m}{\omega_c})^2)$, $b = \sqrt{8a(1 - 2a)}$ and $\omega_c^2 = \frac{2\gamma P}{|\beta_2|} = 4\gamma P k_{wv}$, here in a form with explicit dependency on real world parameters like modulation frequency ω_m and intensity P. The normalized propagation coordinate is $z' = z\gamma P$. The AB in Eq. (15) is a breather with one row of intensity maxima at $z' = 0$ at positions $x = nX$ with an integer n.

Figure 6(a) shows an AB. The row of strongly localized intensity peaks develops from a small sinusoidal symmetric two-sideband input modulation. The growing modulation of the evolving AB equals in fact asymptotically the growing part of the MI solution in Eq. (12). Only for infinite small amplitudes and an exact phase $\varphi = \frac{\psi}{2}$ a pure growing MI solution could grow into a pure AB. However, practically the infinitely long decreasing part of the AB cannot be observed, neither

Optics EXPRESS

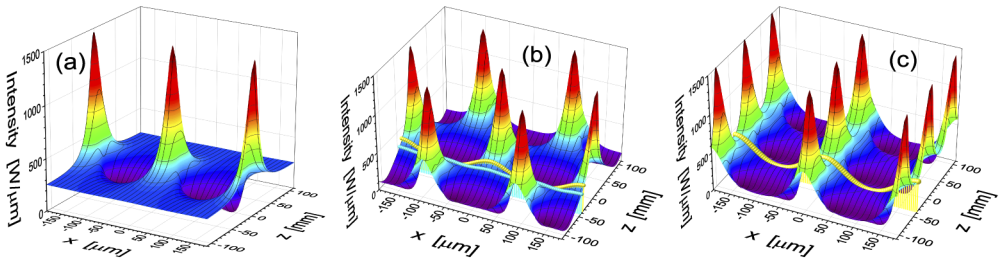

Fig. 6. Breather solutions calculated with Eqs. (16)–(18): (a) Akhmediev breather; (b) A-type breather; (c) B-type breather. $\gamma P = 54.23\,\frac{1}{\mathrm{m}}$, the periodicity 185 μm determines q_0, $\beta_2 = -47.265 \times 10^{-9}$ m, $\gamma = 0.217 \times 10^{-6}\,\frac{1}{\mathrm{m}}$, in (b) and (c) $\kappa = 0.9377$, growing MI eigenmode phase $\frac{\psi}{2} = -44.84°$. The yellow (cyan) dots show symmetric two-sideband modulations with phase $\varphi = -55°$ ($\varphi = -90°$) that would excite the A-type breather in (b) and phase $\varphi = -20°$ that excites the B-type breather in (c) (see the text below).

experimentally nor numerically. The reason is that unavoidable noise components transform the AB into one of the other periodic solutions that are located infinitely close to the AB. The decaying side of the AB always develops MI growing components from noise and imperfections. Repeated rows of maxima develop and the AB is a separatrix between two doubly periodic breather families, type A and type B, with examples shown in Figs. 6(b) and (c). For an input phase $\varphi \neq \frac{\psi}{2}$ the evolving breather type depends on the phase φ in the symmetric two-sideband input $\varepsilon_\mathrm{s} = \varepsilon_\mathrm{a} = \frac{\eta}{2}e^{i\varphi}$.

Like the AB, type A and B breathers are also known analytically [30,31]. The A-type breathers are given by

$$u(x,z) = (-1)q_0\sqrt{P}e^{-iq_0^2z'}\left[\frac{\kappa\mathrm{sn}(\frac{q_0^2z'}{\kappa},\kappa) + iC\mathrm{dn}(\frac{q_0^2z'}{\kappa},\kappa)}{\kappa[1 - C\mathrm{cn}(\frac{q_0^2z'}{\kappa},\kappa)]}\right], \tag{16}$$

with $C(x) = \sqrt{\frac{\kappa}{1+\kappa}}\mathrm{cn}(\sqrt{\frac{P\gamma}{\kappa|\beta_2|}}q_0x, \sqrt{\frac{1-\kappa}{2}})$. With $A(x) = \mathrm{cd}(\sqrt{\frac{P\gamma(1+\kappa)}{2|\beta_2|}}q_0x, \sqrt{\frac{1-\kappa}{1+\kappa}})$ the B type has the form

$$u(x,z) = (-i)q_0\sqrt{P}\kappa e^{-iq_0^2z'}\left[\frac{A\mathrm{cn}(q_0^2z',\kappa) - i\sqrt{1+\kappa}\,\mathrm{sn}(q_0^2z',\kappa)}{\sqrt{1+\kappa} - A\mathrm{dn}(q_0^2z',\kappa)}\right]. \tag{17}$$

With this normalization the AB Eq. (15) has the shorter form

$$u(x,z) = \sqrt{2P}q_0e^{-iq_0^2z'}\left[\frac{-\sqrt{2}\sinh(q_0^2z') - i\cos(\sqrt{\frac{\gamma P}{|\beta_2|}}q_0x)}{2\cosh(q_0^2z') - \sqrt{2}\cos(\sqrt{\frac{\gamma P}{|\beta_2|}}q_0x)}\right]. \tag{18}$$

As in Eq. (15) $z' = z\gamma P$. In these formulas the periodicity is not explicitly accessible but determined by adequate choice of the modulus κ of the Jacobi elliptic functions and the scaling parameter q_0. For a modulus $\kappa = 1$ the period along z of the A- and B-type solutions tends to infinity and Eqs. (16) and (17) become the AB Eq. (18).

A first step towards predicting what kind of breather evolves from a given input was the asymptotic matching of the AB to a growing MI mode for a prediction of the position of the evolving AB maximum in [27]. An extension and completion of the idea was presented in [32]. The intensity peaks of the breathers closely resemble the basic AB in Eq. (15) when they are separated well enough. The valleys between the peaks are approximated by growing and decaying MI solutions of the form of Eq. (12). Therefore a matching of both asymptotic breather tails to an input with modulation of the more general form of Eq. (2) provides a very

Optics EXPRESS

good and versatile tool to predict the propagation starting from an arbitrary sinusoidal input. The recurrence period in z direction as well as the x shift of the maxima from one to the next recurrence row are well described with the formulas in [32] as long as the asymptotic matching procedure provides reasonable results for small enough input modulation amplitudes. These formulas converted to our real-world coordinates predict the distance z_1 from the input to the first maxima row, the distance z_2 between two successive maxima rows and the shift Δ_x of the maxima in two successive rows:

$$z_1 = \frac{2}{\gamma P \sigma} \ln \frac{\sigma^2}{2|\alpha|}, \quad z_2 = \frac{4}{\gamma P \sigma} \ln \frac{\sigma^2}{2\sqrt{|\alpha\beta|}}, \quad \Delta_x = \sqrt{\frac{2|\beta_2|}{\gamma P}} \frac{\arg(\alpha\beta)}{k}. \tag{19}$$

$k = \omega_m \sqrt{\frac{2|\beta_2|}{\gamma P}}$ is a normalized periodicity and determines the parameter $\sigma = k\sqrt{4-k^2}$. $\alpha = \frac{\varepsilon_a^* - \varepsilon_s e^{i\psi}}{\sqrt{P}}$ and $\beta = \frac{\varepsilon_s^* - \varepsilon_a e^{-i\psi}}{\sqrt{P}}$ are calculated from the input modulation.

All breathers in Fig. 6 have at a well defined propagation position z a field that is very similar to $\sqrt{P} + \varepsilon$ with $\varepsilon = \eta e^{i\varphi} \cos(\omega_m x)$. A fit of the breather formulas Eqs. (16) and (17) to that input provides also the breather that would develop from that input. In the examples in Fig. 6 the modulation contrast is $\eta/\sqrt{P} = 0.3$. For an input phase $\varphi < \frac{\psi}{2}$ the input fits to an A-type breather with an example shown in Fig. 6(b). The best fitting input is marked. The same result is obtained from the asymptotic matching procedure. Equations (19) show indeed that an input phase $\varphi < \frac{\psi}{2}$ yields A-type breathers with an x shift of $\frac{X}{2}$ between intensity maxima of successive maxima rows in z direction. An input with a phase $\varphi > \frac{\psi}{2}$ fits best to B-type breathers and also Eqs. (19) predict a breather with no x shift of the intensity maxima as shown in Fig. 6(c), with the best fit marked. A maximum 3 % variation of κ in the fitting is neglected in the breather plots which are all shown for $\kappa = 0.9377$. Figure 7 compares predicted distances between input and the first row of breather maxima dependent on modulation amplitude η and phase φ, found from fitting, asymptotic matching and numerical simulation. Considering experimental tolerances all three predictions give the same results as long as for small modulation amplitudes $\frac{\eta}{\sqrt{P}} < 0.3$ the breather fields contain a portion that fits well to a cosine modulation.

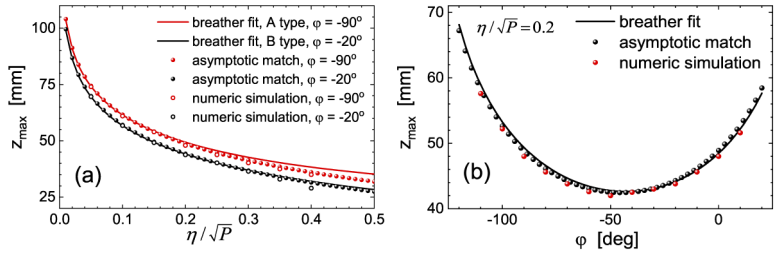

Fig. 7. Distance z_{max} between excitation and first row of breather maxima for the breathers with parameters shown in Fig. (6): (a) dependent on modulation amplitude $\frac{\eta}{\sqrt{P}}$; (b) dependent on modulation phase φ.

Showing the phase trajectories of a scaled complex field $U(z) = \frac{u(0,z)}{1000} e^{iq_0^2 z'}$ along a row of maxima in the complex plane, the phase-dependent breather selection is alternatively visualized in Fig. 8. The factor $e^{iq_0^2 z'}$ eliminates the fast oscillations. The trajectory direction is marked for increasing z from $-\infty$ to $+\infty$. The point $U(-\infty) = \frac{\sqrt{P}+0j}{1000}$ corresponds to a plane wave (here with $P \times 1 \frac{W}{m} = 250 \frac{W}{\mu m}$). Adding a small perturbation $\varepsilon(x=0) = \eta e^{j\varphi}$ with the correct asymptotic AB phase $\varphi = \frac{\psi}{2}$, a starting point on the AB trajectory is obtained (black arrow in right Fig. 8). For a smaller phase $\varphi < \frac{\psi}{2}$ a starting point on a trajectory of an A-type breather is reached (red

Optics EXPRESS

arrow) and for $\varphi > \frac{\psi}{2}$ a B-type breather trajectory is started (green arrow). It is important to note that the phase trajectories in Fig. 8 are plotted for breathers with the same x periodicity.

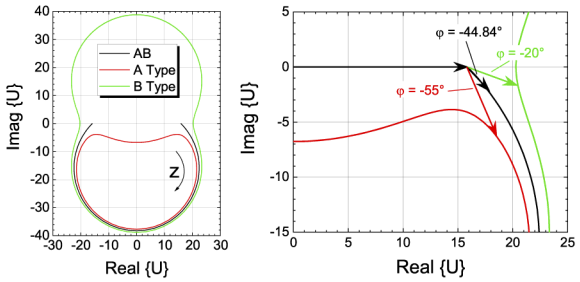

Fig. 8. Phase trajectories $U(z)$ of breathers from Fig. 6. The magnified view on the right shows the excitation with different modulation phases $\varphi = \frac{\psi}{2} = -44.84°, \varphi = -55°$ and $\varphi = -20°$.

Non-symmetric or even one-sideband input modulation yield moving breathers (see Fig. 9). The maxima resemble straight propagating ABs with "tilted valleys" in between. The superposition of growing and decaying MI introduces the tilt due to the shift of their modulation patterns. Also for the tilted or moving breathers analytical solutions are known [8,33]. The discussion from above on trajectories and fitting of input perturbations to breather fields could be tried for non-symmetric input as well. However, our experimental work is perfectly explained by the asymptotic matching analysis from [32] and by numerical simulations. So we skip the very long formulas on tilted breathers in this manuscript. For the one-sideband modulation $\varepsilon(x, z = 0) = \eta e^{i0^\circ} e^{i\omega_m x}$ with the parameters for Fig. 9, Eqs. (19) yield a row of first localizations at $z_1 = 55.24$ mm, a shift of the maxima between successive rows of $\Delta_x = -46.41\ \mu$m and a periodicity of $z_2 = 110.48$ mm in very good agreement to the numeric results. In Fig. 9 the $z_{1,2}$ values are 0.5 % smaller and the Δ_x shift is 1.5 % larger.

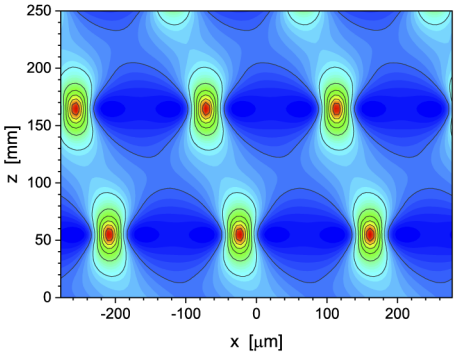

Fig. 9. Numerical simulation of a moving breather with one-sideband input. $\gamma P = 54.23\ \frac{1}{\mathrm{m}}$, $\beta_2 = -47.265 \times 10^{-9}$ m, $\omega_m = \frac{2\pi}{185\,\mu\mathrm{m}}$, $\frac{\eta}{\sqrt{P}} = 0.1$.

With the far developed breather excitation methods in fiber experiments, tilted breathers have been generated in very good quality and used for interaction investigations [19,21].

3. Characterization of nonlinear beams with intensity scans

In experiments with access to only input and output intensity profiles of the nonlinear beam, the output can be observed dependent on a parameter, easiest on the input intensity. Also the

Optics EXPRESS

modulation frequency, modulation depth, type of modulation or the nonlinearity can be changed, but are fixed in an intensity scan. The output intensity is measured for increasing input intensity. Each output is normalized to its power and composed into a figure showing the normalized output versus input intensity. Resulting intensity scans are shown in Fig. 1 for experimental data and in Figs. 10, 11 and 12 for simulations. An intensity scan illustrates the whole intensity dependence of a nonlinear beam propagation in one figure. However, the parameters of intensity scans need to be chosen very carefully to characterize MI or show specific breathers. Because the phase $\frac{\psi}{2}$ of the MI eigensolution is intensity-dependent (example shown in Fig. 11(c)), a localization in an intensity scan is not an exact picture of one specific breather but resembles a breather in more or less good approximation as a collection of scans through similar breathers.

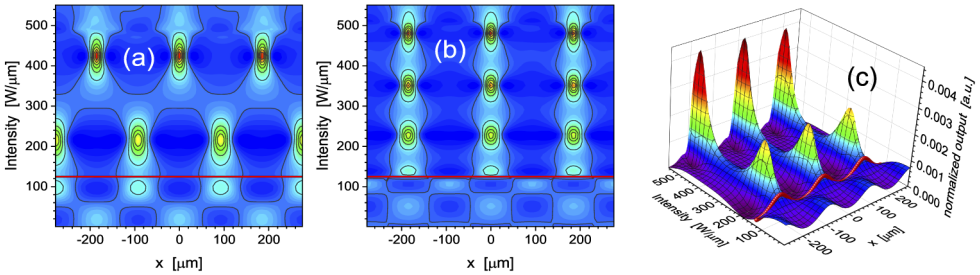

Fig. 10. Intensity scans for symmetric two-sideband input modulation: (a) sample length $L = 150\,\mathrm{mm}$, $\varphi = -80° < \frac{\psi}{2}$; (b) $L = 150\,\mathrm{mm}$, $\varphi = 0° > \frac{\psi}{2}$; (c) $L = 60\,\mathrm{mm}$, $\varphi = 0° > \frac{\psi}{2}$. The red line marks P_c. Nonlinearity $\gamma = 0.217 \times 10^{-6}\,\frac{1}{\mathrm{m}}$, diffraction $\beta_2 = -47.265 \times 10^{-9}\,\mathrm{m}$, modulation frequency $\omega_\mathrm{m} = \frac{2\pi}{185\,\mu\mathrm{m}}$, relative modulation field amplitude $\frac{\eta}{\sqrt{P}} = 0.24$.

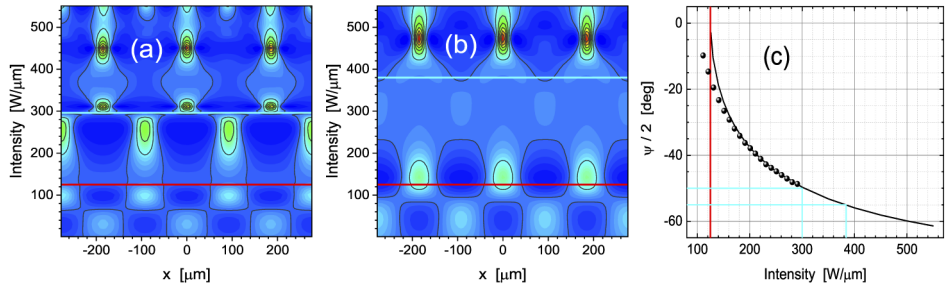

Fig. 11. Intensity scans for symmetric two-sideband input modulation with phase transition at the cyan line: (a) $L = 150\,\mathrm{mm}$, $\varphi = -50°$; (b) $L = 90\,\mathrm{mm}$, $\varphi = -55°$; (c) MI eigenmode phase $\frac{\psi}{2}$ versus input intensity. The dots compare eigenmode phases extracted from the fringe shift in a one-sideband modulation, explained in the next section. The red line marks P_c. $\gamma = 0.217 \times 10^{-6}\,\frac{1}{\mathrm{m}}$, $\beta_2 = -47.265 \times 10^{-9}\,\mathrm{m}$, $\omega_\mathrm{m} = \frac{2\pi}{185\,\mu\mathrm{m}}$, $\frac{\eta}{\sqrt{P}} = 0.24$.

For intensities below the MI threshold P_c, the intensity-dependent increase of the Talbot periodicity determines the scan. In Figs. 10, 11 and 12 P_c is marked with a red line. Above P_c breathers appear with growing and decaying MI at their flanks. With increasing intensity the breather maxima move toward the input facet and at the output we scan different rows of maxima. In intensity scans with more rows, intensity-dependent modifications of the AB are observable. Higher-power ABs are narrower with higher relative peak intensity and stronger localization. For a phase of the symmetric two-sideband modulation $\varphi < \frac{\psi}{2}$ A-type and for $\varphi > \frac{\psi}{2}$ B-type breathers develop, as shown in Figs. 10(a) and 10(b), respectively. Here we observe scans only through second and higher rows of breather maxima. In such long samples the first breather maximum

Optics EXPRESS

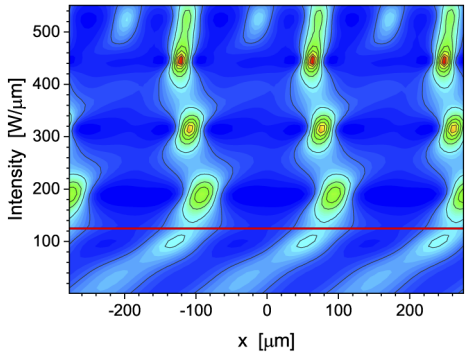

Fig. 12. Intensity scan for one-sideband input modulation. The red line marks P_c. Sample length $L = 150\,\mathrm{mm}$, $\varphi = 0°$, nonlinearity $\gamma = 0.217 \times 10^{-6}\,\frac{1}{\mathrm{m}}$, diffraction $\beta_2 = -47.265 \times 10^{-9}\,\mathrm{m}$, modulation $\omega_\mathrm{m} = \frac{2\pi}{185\,\mu\mathrm{m}}$, relative modulation field amplitude $\frac{\eta}{\sqrt{P}} = 0.24$.

develops even at small intensities inside the crystal and cannot be observed at the output. To visualize the first row of breather peaks in the intensity scan, they need to be shifted to the output facet of the crystal, either by reducing the modulation amplitude or by using a shorter sample. In Fig. 10(c) the first and second row of the breather maxima are seen in a shorter sample. A decision on the peak number of the breather is easiest to find from evolution pictures versus propagation coordinate z like Figs. (6) or (9). The sample length influences also the observable Talbot regime at the beginning of the scan. Experimentally this seems similar to the observations in [15].

The scans can show many interesting scenarios. For a suitable input phase φ a switching from an A- to a B-type breather can be observed in one intensity scan. In Fig. 11(a) at exactly that intensity level where the intensity-dependent asymptotic breather phase $\frac{\psi}{2}$ switches from $\frac{\psi}{2} > \varphi$ to $\frac{\psi}{2} < \varphi$ (marked with a cyan line), a corresponding transversal jump of the maximum by half a modulation period is observed. Here the switching occurs at an intensity where a peak of the breather is localized at the end of the crystal. Changing the sample length, the switching in Fig. 11(b) occurs when the localization is relaxed at the output and a more flat region separates A- and B-type regions in the scan.

For a one-sideband modulation the situation becomes much simpler but less versatile because the phase is no longer determining the behavior. However, Talbot effect, MI and breathers are all accessible. Figure 12 shows an example with behavior comparable to Fig. 10(b). The back-shifting of the moving interference fringes from low to MI intensity levels is well pronounced with the predicted phase from Eq. (14), and confirmed experimentally (see Fig. 1 and experimental section). The different rows of breather maxima for increasing intensity are shifted transversely due to the input tilt according to the x-shift Δ_x from Eq. (19). The small tilt of each single breather maximum is attributed to the intensity dependence of the angle ψ. Because of the decreasing slope of the dependency (see Fig. 11(c)), the tilt diminishes for larger intensity. The input phase only shifts the whole pattern horizontally.

3.1. Breather characterization

Considering the normalization of the propagation coordinate $z' = z\gamma P$, it is even possible to gain information on the propagation of a breather inside the sample by scanning z' with P instead of z, as we do it in the intensity scan and as it was similarly done by scanning γ in [15]. However, this is only an approximation because with P other breather parameters change as well, and not only

Optics EXPRESS

z' (a, b and the asymptotic phase $\frac{\psi}{2}$ in Eq. (15)). The approximation is in certain limits not bad if we compare localized intensity peaks versus z'. In Fig. 13(a) we see an intensity scan plotted versus $z' = z\gamma P$ at fixed z. In the range of the breather maximum $3<z'<5$, the breather parameters vary in the ranges $0.227<a<0.339$, $0.997>b>0.935$ and $-42°>\frac{\psi}{2}>-55°$. Figure 13(b) shows a propagating breather versus $z' = z\gamma P$ with fixed P and growing z. The parameters $a = 0.291$, $b = 0.987$ and $\frac{\psi}{2} = -49.7°$ are fixed. The parameter variations in Fig. 13(a) are small and the peak bears a very strong resemblance to the AB evolution in Fig. 13(b). The change of $\frac{\psi}{2}$ with intensity is the only detectable small difference observable in the contour lines in Figs. 13(a) and (b). Considering the experimental accuracy, breather maxima can be characterized well with intensity scans.

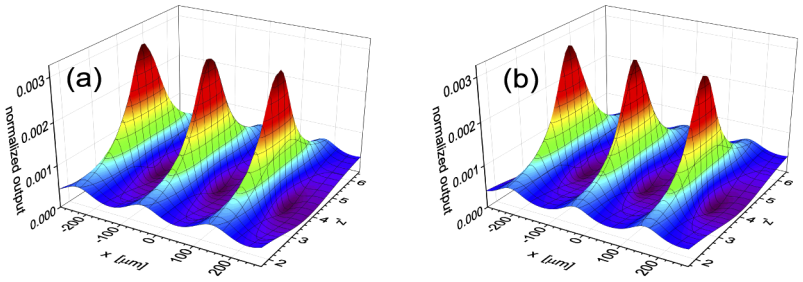

Fig. 13. Comparison of an intensity scan and a breather, both plotted versus normalized propagation coordinate $z' = z\gamma P$: (a) intensity scan from $P = 130$ to 500×10^6, $z = 60$ mm; (b) breather evolution, $P = 300 \times 10^6$, $z = 26$ to 100 mm. $\gamma = 0.217 \times 10^{-6}\,\frac{1}{\mathrm{m}}$, $\beta_2 = -47.265 \times 10^{-9}$ m, $\omega_\mathrm{m} = \frac{2\pi}{185\,\mu\mathrm{m}}$, $\frac{\eta}{\sqrt{P}} = 0.035$.

3.2. MI gain measurement

In the regions between the breather maxima, MI determines the field evolution. From the growing and decaying breather flanks, information on the growth and decay rates of MI can be collected. It is straightforward to determine the MI gain rate from the MI regime before the first breather localization in the intensity scans. The gain factor is accessible from comparing the modulation amplitudes of scans at low intensity in the linear Talbot-effect regime and scans at intensities below the first breather maximum where MI approximates the field evolution. However, a careful parameter selection is necessary to identify the appropriate MI regime, to suppress the decaying MI contribution and evaluate only the growing MI mode in Eq. (12). With a symmetric two-sideband modulation, a correct phase between the seed and the background would satisfy this condition exactly. With a one-sideband modulation the phase control is not necessary. Both, decaying and growing MI modes are triggered equally strong. The gain can be determined from the growth of the growing mode when the decaying mode becomes small enough at the sample end. Figure 14 shows corresponding data. The marked output scans in Fig. 14(a) are compared in Fig. 14(b) with their first harmonic. Because the moving fringe pattern due to the tilted input is shifted back at MI intensities, an output fringe phase of $\frac{\psi}{2} + \frac{\pi}{2}$ is an indication for a strong enough decay of the decaying mode. From the actual shift of the fringes, $\frac{\psi}{2}$ is extracted which fits very well the calculated eigenmode phases in Fig. 11(c). The input and output intensities for the one-sideband modulation are proportional to $|E(z=0)|^2 = P + 2\sqrt{P}\eta\cos(\omega_\mathrm{m}x) + \eta^2$ and $|E(z=L)|^2 = P + \frac{2\sqrt{P}\eta e^{gL}}{|\sin\psi|}\cos\frac{\psi}{2}\cos(\omega_\mathrm{m}x + \frac{\psi}{2} + \frac{\pi}{2}) + \frac{\eta^2 e^{2gL}}{\sin^2\psi}\cos^2(\omega_\mathrm{m}x + \frac{\psi}{2} + \frac{\pi}{2})$. L is the sample length. The Fourier transforms of the intensity scans in Fig. 14(b) provide the amplitudes $A_\mathrm{in} = 2\sqrt{P}\eta$ and $A_\mathrm{out} = \frac{2\sqrt{P}\eta e^{gL}}{|\sin\psi|}\cos\frac{\psi}{2}$ of the modulation at the different intensities which are

Optics EXPRESS

used for calculating the gain values $g = \frac{1}{L} \ln \frac{A_{\text{out}} |\sin \psi|}{A_{\text{in}} \cos \frac{\psi}{2}}$ in Fig. 14(c). The theoretical gain curve from simple MI theory is plotted for comparison. The validity range for the MI description ends at the high intensity side with the development of a breather. The gain measurement yields too small gain factors for intensities too close to the breather maximum. At the low intensity side, but still above the Talbot regime, the decaying mode may still be present and distorts the result with too large values for the gain. In an experiment it is important to select parameters for a wide enough window where the MI description is valid. For intensities in the Talbot regime left of the red line in Fig. 14(c), a gain measurement does not make any sense and the up and down of the periodic localizations from Fig. 3 are observed.

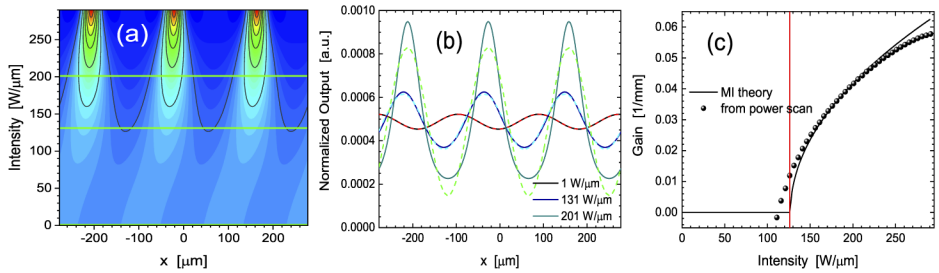

Fig. 14. MI gain extracted from an intensity scan with one-sideband modulation: (a) intensity scan, $L = 60$ mm; (b) scans through intensity scan (solid) at intensities marked with green lines in (a) compared to their first harmonic (dashed); (c) from harmonic amplitudes calculated gain factor (scattered) compared to the calculated gain from MI theory (solid). $\gamma = 0.217 \times 10^{-6} \frac{1}{\text{m}}$, $\beta_2 = -47.265 \times 10^{-9}$ m, $\omega_{\text{m}} = \frac{2\pi}{185\,\mu\text{m}}$, $\frac{\eta}{\sqrt{P}} = 0.035$.

4. Experimental results

4.1. Experimental system

Till now we do not know about a real 1D nonlinear beam propagation experiment in the ps-regime based solely on the fast intrinsic cubic electronic Kerr nonlinearity $\chi^{(3)}$, except for a few early spatial soliton experiments in AlGaAs [34]. The intrinsic cubic electronic nonlinearity is too small in common crystals to observe nonlinear beam propagation up to intensities necessary for the MI or even breather regime without endangering the crystal. Instead, numerous and extensive studies of nonlinear beam propagation based on slower but stronger cubic nonlinearity replacements have been performed in photorefractive materials or in liquid crystals with orientation effects [15,25,35]. The only option for mimicking a pure cubic nonlinearity with relatively fast time response is the use of a cascaded second-order $\chi^{(2)} : \chi^{(2)}$ nonlinearity [36]. Operated far from phase-matching of the underlying second-order frequency mixing, the cascaded nonlinearity is experimentally hard to distinguish from the real electronic Kerr nonlinearity for ps-pulses. From soliton experiments [37] through MI [5] to breather investigations [16] the interesting range of nonlinear beam propagation had been covered based on cascading.

For an experimental verification of the previous theoretical considerations we used a mixture of the electronic $\chi^{(3)}$ and the cascaded nonlinearity in the $\chi^{(3)}$-like limit in a slab waveguide on a Y-cut $LiNbO_3$ crystal. The waveguide with a length $L = 47$ mm was fabricated in the 1990s by Wolfgang Sohler's group in Paderborn for the experimental demonstration of quadratic solitons [37] and MI measurements [5]. Type I second-harmonic generation (SHG) can be implemented by coupling a fundamental frequency (FF) ordinary polarized TM_0 mode at a wavelength of 1.32 μm to extraordinary TE modes at the second-harmonic (SH) frequency at a wavelength of 0.66 μm. Temperature tuned, birefringent phase-matching occurs at 297 °C to the TE_0 mode and

Optics EXPRESS

at 344 °C to the TE_1 mode. The phase-matching temperature in our crystal has increased by ≈ 8 Kelvin during the last 25 years [37]. For controlling phase-matching, the crystal was housed in an oven. The waves propagate along z (crystallographic X) direction, are guided along the y (Y) coordinate, and the light localization is observed in x (Z) direction. The diffraction term for the FF TM_0 mode is $\beta_2 = -47.265 \times 10^{-9}$ m. More details on the waveguides with cascading driven by SHG are found in [5,16,37,38].

The effective cubic $\chi^{(3)}$-like nonlinearity of the two resonances plus the intrinsic electronic $\chi^{(3)}$ are shown in Fig. 15. For an operation ≈ ±10 K from the SHG resonances outside the shaded regions we can describe the $\chi^{(3)}$-like system for our experimentally covered intensity range in very good approximation with the NLSE Eq. (1). Experimentally we confirmed the $\chi^{(3)}$-like system by checking that the output SH is negligible compared to the FF. Note that the nonlinearity can be adjusted from $\gamma = 0$ to $0.6 \times 10^{-6}\,\frac{1}{\mathrm{m}}$.

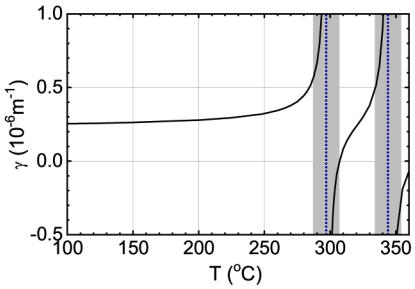

Fig. 15. Total cubic nonlinearity $\gamma = \sum_{\nu=1}^{2} \frac{1}{\Delta k_\nu} \left(\frac{\omega_1 K_\nu^{(2)} 2d}{4p_0} \right)^2 + \frac{\omega_1 K^{(3)} \chi^{(3)}}{4p_0}$ consisting of a temperature-tunable cascading part and a constant intrinsic part with ν denoting the SH resonance. Δk_ν is the temperature-dependent wave-vector mismatch, ω_1 is the laser frequency, $K_\nu^{(2)}$ and $K^{(3)}$ are mode-overlap integrals. d and $\chi^{(3)}$ are electronic second- and third-order susceptibilities. Numbers are found in [16].

The experimental setup is shown in Fig. 16. The light source was a frequency-doubled Nd:YAG-pumped OPA with cw-seeding delivering 5.5-ps-long pulses at a wavelength of 1.32 μm with up to 450 kW peak power. With a cylindrical telescope the laser beam was transformed into a very wide Gaussian elliptical beam (1.4 mm × 8 μm) providing the background. The beam was end-fire coupled into the FF TM_0 mode. Power scaling with calibrated power meters enabled absolute measurements of the average input power. The input power is converted to the temporal peak intensity I_P in the mode in the center of the input beam. A few percent of the FF beam were separated after the telescope and coupled with a tilt and good overlap to the main FF beam into the waveguide. The interference between the two FF beams produced a spatial one-sideband modulation of the input with adjustable period and modulation depth $m = (I_{1,\,\mathrm{max}} - I_{1,\,\mathrm{min}})/I_{1,\,\mathrm{max}}$. The beam width of 1.4 mm along the x coordinate can be considered large enough in the compromise between available power and infinite beam width so that a FF beam with a transverse modulation with periods between 130 and 300 μm well approximates a quasi-constant background with a harmonic modulation.

4.2. Intensity scans and breathers

We measured a few hundred intensity scans with different periodicity, modulation depth and nonlinearity to document experimentally the variety of the theoretical predictions with exemplary results in Fig. 17. Figure 17(a) shows a completely intensity-independent propagation for a vanishing nonlinearity at 307 °C. The cubic and the cascaded nonlinearities from the two SH resonances cancel exactly at this temperature and the system behaves linear in the regime of

Optics EXPRESS

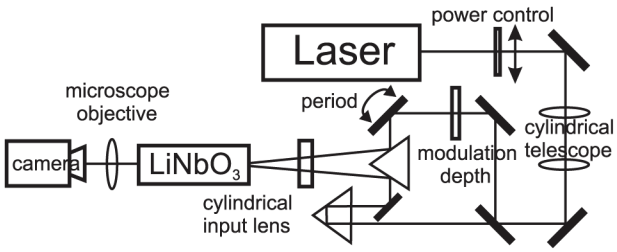

Fig. 16. Experimental setup.

balancing competing nonlinearities [39] in the whole available power range. The nonlinear modifications of the Talbot effect are observable in the low-intensity regime in Figs. 17(b) and 1(b). For the shortest modulation period of 133 μm we can exactly observe the scenario from Fig. 3 in our 47-mm-long sample with intensity-dependent beam shift and periodic up and down of the peak intensity before the MI threshold. For larger periodicity the start of MI leaves no space for the decreasing part of the Talbot pattern and a monotonic modulation increase develops directly into MI and breathers (see Figs. 17(c) and 1(a)). Figure 17(c) shows such an Akhmediev breather scan. In a longer sample, a recurrence in form of a second row of breather maxima could be observed. However, higher intensity or an increase of the nonlinearity by operating closer to phase-matching did not generate further recurrences. Instead, Fig. 17(d) shows strong disturbances in the breather decay after a quickly developing first breather maximum. The spatial second harmonic of the modulation experiences MI gain and higher-order breathers interfere with the recurrence of the first-order breather. In fact, at 342.2 °C, so close to the second phase-matching resonance, the validity of the $\chi^{(3)}$ approximation with the NLSE fades and the complete SHG equations (see [16]) were used for a better simulation of this real quadratic cascading regime. The system becomes very sensitive to input conditions and deviates from a pure NLSE system after the first breather maximum.

In the growing part of the developing intensity peaks in Figs. 17 we can identify in all scans the MI regime. The peak intensity for a start of MI is marked in the scans with a red line. The MI regime ends when MI saturates at intensities below the breather peak.

Another try to observe the second recurrence of breather maxima was a shift of the breather towards lower intensities by increasing the modulation strength. To avoid amplification of second-order breathers, the small modulation period of 133 μm was used. Figure 18 shows a typical result. The Talbot regime ends at the onset of MI close to the line at 100 $\frac{\mathrm{W}}{\mu\mathrm{m}}$. Indeed, above this intensity a breather with a first row of maxima inside the sample propagates with the decaying breather wing in the intensity scan following directly the Talbot regime. A window for an observation of growing MI is not available in this scan. Only at the end of the scan (beyond our available intensity) the beginning of the second row of breather maxima appears. All intensity scans with 133 μm period and the largest modulation contrast $\frac{\eta}{\sqrt{P}} = 0.24$ show similar smooth fringes without developed maxima. The power-dependent x-shift yields the well observable snake-like fringes.

All our scans agree qualitatively and in 80 % of the scans without any parameter fit even quantitatively very well to the theory when we allow a zero to −15 % uncertainty of the power in the waveguide due to laser adjustment and coupling uncertainty. In the remaining 20 % of scans the experimental power in the waveguide can be up to 30 % too small which is due to the experimental challenge to operate the laser over the measuring period of one year at exactly the same setting. In a few scans, when the environment was not stable, a fluctuation of the phase of the seeding leads to fringe position fluctuations yielding a jitter in the modulation and noisy MI gain measurements.

Optics EXPRESS

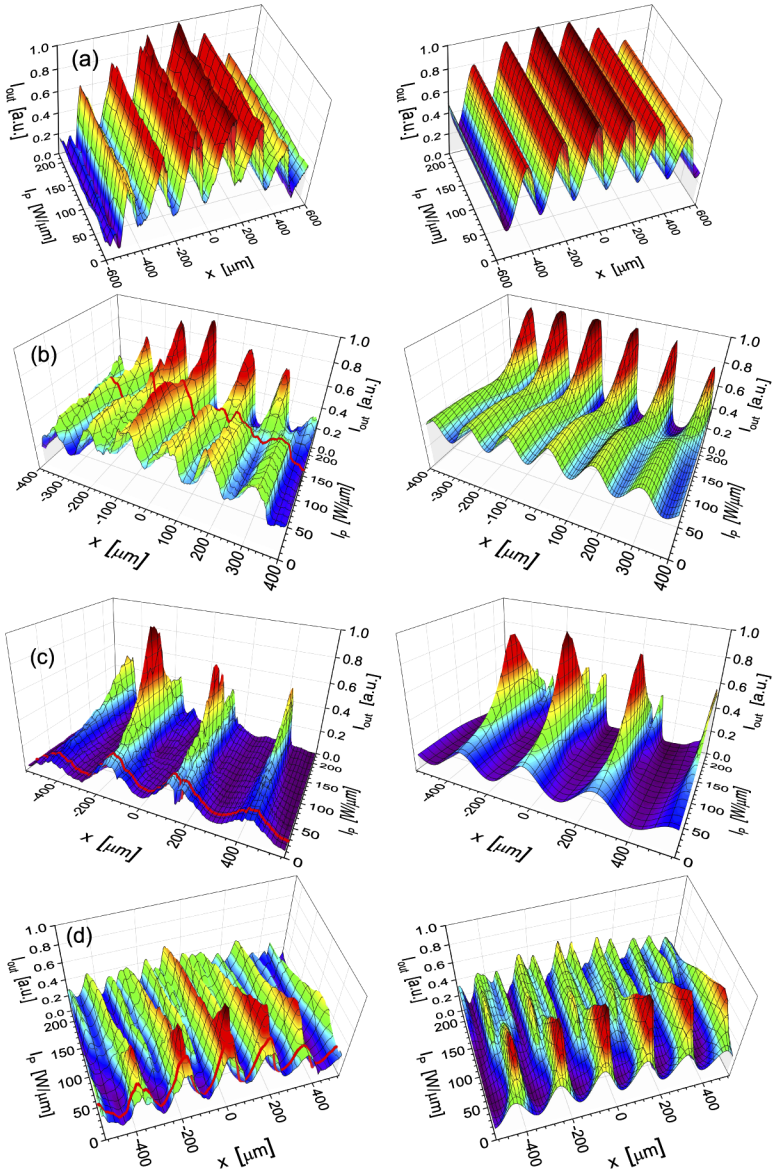

Fig. 17. Measured intensity scans with one-sideband modulation (left) compared to calculations (right): (a) balanced nonlinearity at 307 °C, $\omega_{\mathrm{m}} = \frac{2\pi}{185\,\mu\mathrm{m}}$, $\frac{\eta}{\sqrt{P}} = 0.24$; (b) nonlinear modified Talbot pattern at 280 °C, $\omega_{\mathrm{m}} = \frac{2\pi}{133\,\mu\mathrm{m}}$, $\frac{\eta}{\sqrt{P}} = 0.11$; (c) first row of breather maxima at 285 °C, $\omega_{\mathrm{m}} = \frac{2\pi}{300\,\mu\mathrm{m}}$, $\frac{\eta}{\sqrt{P}} = 0.24$; (d) disturbed breather decay at 342.2 °C, $\omega_{\mathrm{m}} = \frac{2\pi}{185\,\mu\mathrm{m}}$, $\frac{\eta}{\sqrt{P}} = 0.24$. I_{P} is the peak intensity of the input pulses.

Optics EXPRESS

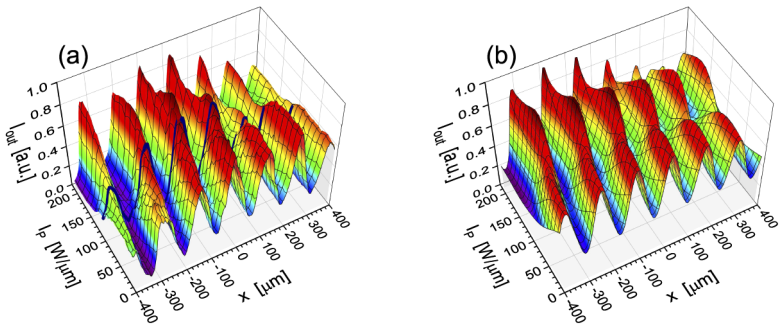

Fig. 18. Snake-like intensity scans without well expressed peaks, one-sideband modulation: (a) measured; (b) calculation. 287.5 °C corresponds to a nonlinearity $\gamma = 0.58 \times 10^{-6}\,\frac{1}{\mathrm{m}}$, $\omega_\mathrm{m} = \frac{2\pi}{133\,\mu\mathrm{m}}$, $\frac{\eta}{\sqrt{P}} = 0.24$. The dark blue line indicates the end of the Talbot regime.

For the theoretical simulation of the experimental data we have used a simple time averaging over the 5.5-ps-long pulse. Except for the simulation in Fig. 17(d), all simulations based on the NLSE and the strict SHG cascading equations give the same pictures. As time resolved calculations confirmed, dispersive effects are negligible in the regime of an effective cubic nonlinearity outside the shaded regions in Fig. 15.

4.3. Breather spectra

The triangular shape of the logarithmic spectral intensity as a unique feature of an AB was measured in nonlinear pulse experiments with an optical spectrum analyser in superior resolution [10,17,40]. According to Fourier Optics [1], the spatial spectrum is detected in the nonlinear beam propagation experiment in a camera with a simple modification of the imaging geometry. With a lens in a distance from the waveguide output equal to the focal length, the spatial spectrum is seen in the camera far behind the lens. Figure 19 shows the evolution of the spatial spectra of the output depending on the input intensity I_P. The corresponding intensity scan looks similar to Fig. 20(a), but reaches the first breather maximum at $I_\mathrm{P} = 270\,\frac{\mathrm{W}}{\mu\mathrm{m}}$. So the spectrum at the end of the scan represents the spectrum of the breather maximum. The intensity spectral scan in Fig. 19(a) shows the four-wave-mixing generation of the triangular shaped spectral lines of the breather, starting from the two input lines of the one-sideband input for increasing I_P. At $\Omega = -3.33\,\mathrm{mm}^{-1}$ the input modulation sideband develops into the first negative-side line. At $\Omega = +3.33\,\mathrm{mm}^{-1}$ the first positive-side line develops from a zero input. Figure 19(b) shows the development of the power of the spectral side lines towards the triangular shape.

4.4. MI gain

From the intensity scans the gain of MI is extracted as discussed in the theoretical section 3.2. For a modulation period of 200 μm and larger, the procedure gives easily very reliable results from a large and good accessible MI regime between Talbot pattern and first breather maximum in our 47-mm-long crystal with experimentally convenient modulation contrast. An example for $\omega_\mathrm{m} = \frac{2\pi}{300\,\mu\mathrm{m}}$ is presented in Fig. 20. The intensity scan in Fig. 20(a) shows a clean exponential modulation growth in the whole range from the MI threshold of 30 $\frac{\mathrm{W}}{\mu\mathrm{m}}$ to the maximum intensity 230 $\frac{\mathrm{W}}{\mu\mathrm{m}}$. A few scans for calculating the modulation amplitudes are marked with green lines. From the ratio of the output- and input-modulation amplitudes an uncorrected gain $g = \frac{1}{L}\ln\frac{A_\mathrm{out}}{A_\mathrm{in}}$ is calculated and plotted in Fig. 20(b) with green stars. The observable x-shift of the maxima in Fig. 20(a) yields the eigenmode phase $\frac{\psi}{2}$ dependent on intensity. The good agreement to the cw

Optics EXPRESS

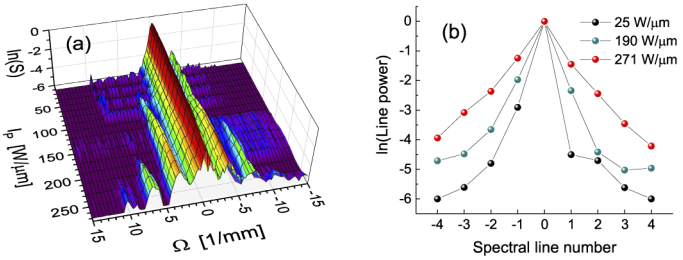

Fig. 19. Logarithmic normalized spatial output spectra: (a) intensity spectral scan ln(S) versus peak input intensity I_P, Ω is the spatial frequency; (b) power in the spectral lines at the output for $I_P = 25, 190$ and $271\ \frac{W}{\mu m}$. Sample temperature of 240 °C, $\omega_m = \frac{2\pi}{300\,\mu m}$, modulation contrast $\frac{\eta}{\sqrt{P}} = 0.11$.

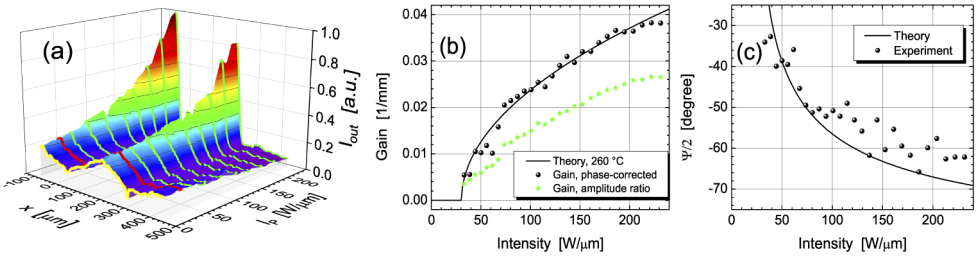

Fig. 20. MI gain extracted from an intensity scan with one-sideband modulation: (a) intensity scan with marked scans for minimum intensity (yellow), MI threshold (red) and gain calculation (green); (b) phase-corrected (black dots) and raw gain (green stars) compared to a cw-gain curve (reduced by 0.75); (c) measured eigenmode phase $\frac{\psi}{2}$ compared to cw theory. Sample temperature of 260 °C corresponds to a nonlinearity $\gamma = 0.35 \times 10^{-6}\ \frac{1}{m}$, $\omega_m = \frac{2\pi}{300\,\mu m}$, modulation contrast $\frac{\eta}{\sqrt{P}} = 0.11$.

calculation is visualized in Fig. 20(c). With the phase correction the final gain $g = \frac{1}{L} \ln \frac{A_{out}\,|\sin\psi|}{A_{in} \cos\frac{\psi}{2}}$ is found in very good agreement to the theoretical gain curve (see Fig. 20(b)). Because of the pulsed experiments, the theoretical cw gain needs to be reduced by a factor of ≈ 0.75 to represent the pulsed experimental results.

The expected nonlinearity and periodicity dependence of the gain curves was confirmed. For smaller nonlinearity a decreasing gain and an increasing MI threshold are observed in Fig. 21(a). Also the effect of MI saturation is detected when an increase of the modulation contrast ratio to $k = \frac{\eta}{\sqrt{P}} = 0.24$ shortens the MI range by shifting the breather formation towards lower intensities. Above intensities of $100\ \frac{W}{\mu m}$ a breather forms and the MI gain calculation gives declining values for intensities above the breather maximum (see blue dots in Fig. 21(a)). Decreasing the periodicity yields an increase of the MI threshold and the slope of the gain curve increases as shown in Fig. 21(b).

However, in our 47-mm-long sample the gain measurement comes to its limit at modulation periods around 140 μm and below, as noisy data in Fig. 21(b) suggest. For a period of 133 μm only a very small MI range window remains between a pronounced Talbot pattern and MI saturation with breather formation, as observable in Fig. 17(b). For smaller modulation periodicity our sample is too long for a good MI measurement (see Fig. 18). A reduction of the modulation contrast would shift the breather maxima towards higher intensity or a reduction of the sample length would shorten the Talbot regime and reopen the window. The possibility of reducing the

Optics EXPRESS

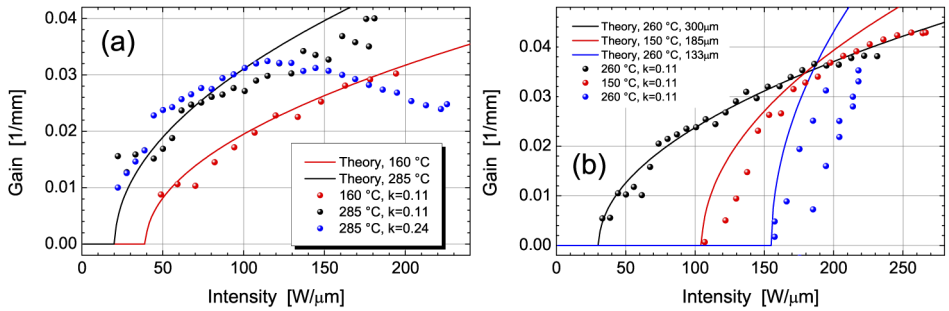

Fig. 21. Phase-corrected MI gain extracted from intensity scans with one-sideband modulation compared to cw-gain curves (reduced by 0.75): (a) nonlinearity $\gamma = 0.27\times10^{-6}\ \frac{1}{\mathrm{m}}$ at 160 °C (red), $\gamma = 0.52\times10^{-6}\ \frac{1}{\mathrm{m}}$ at 285 °C (black) for $k = 0.11$ and for $k = 0.24$ (blue dots), $\omega_{\mathrm{m}} = \frac{2\pi}{300\,\mu\mathrm{m}}$; (b) $k = 0.11$ and different modulation periods 300 μm (black), 185 μm (red) and 133 μm (blue).

modulation contrast is limited because for a modulation contrast below $k = 0.03$ imperfections in the input beam and the sample have the same order of magnitude as the modulation and disturb triggered MI. A shorter sample was not available. Thus, for the shortest periodicity of 133 μm we could not observe better results than those shown in Fig. 21(b) in blue. The results are reproduced by simulations confirming that the geometry (periodicity, modulation contrast and sample length) determines the parameter range for possible gain measurements.

5. Conclusion

A theoretical introduction with repetition of well known MI theory and breather formulas provides a consistent basis for a discussion of nonlinear beam propagation measurements. It proved to be a complete basis, because all the preparation, processing, simulation and interpretation of my experimental work on nonlinear beam propagation, especially MI and breather formation, was based solely on the herein presented formulas and terms. Of course, the summary on MI and breathers is nothing but an extract and translation of the extensive literature and conversion to uniform definitions and language.

We extended our old platform for investigating nonlinear beams to experiments on breathers and growing and decaying MI. The nonlinear medium is a film waveguide to apply the NLSE for beam propagation in one transverse and one longitudinal spatial direction. A mixture of the electronic cubic and cascaded quadratic nonlinearity in SHG was used for realization of an adjustable effective cubic nonlinearity. The cascaded nonlinearity was operated far from phase-matching in the $\chi^{(3)}$-like limit so that theory is based in good approximation on the NLSE.

The experimental demonstration of nonlinear modifications of the Talbot effect, MI growth, breather formation and MI decay was successful. For the presentation of nonlinear beam propagation a form with intensity scans was meticulously elaborated. Breathers could be characterized. MI was quantified with gain measurements. The differences to a direct observation of z-dependent propagation were discussed as well as drawbacks, limits and advantages.

Our system is good for an observation and characterization of one breather cycle. A breather recurrence or a second row of breather maxima could not be observed, our sample was too short for the available parameters as modulation period, amplitude, and power. For measurements of nonlinear material properties, here the electronic cubic $\chi^{(3)}$, a measurement of the appearance of the first breather maximum is very useful. In case of additional quadratic cascading, the resulting only effective $\chi^{(3)}$ can easily be corrected for the quadratic cascaded effect with the knowledge of the second-order susceptibilities. The MI gain can also be used for nonlinearity measurements.

Optics EXPRESS

However, this measurement is less favorable because it depends on the modulation growth and the correction with the eigenmode phase. Only under limited conditions both are observable precisely enough.

A direct comparison with our old MI gain measurements in [5] is not possible because of different parameter ranges. Here we work under $\chi^{(3)}$-like conditions. In [5] MI of quadratic eigenmodes close to phase-matching was characterized. However, remembering the good agreement of the presented measurements and theory we could apply the NLSE-based theory to those old data (from [5]) closest to the $\chi^{(3)}$ limit. Considering that in the old work the phase-correction for the gain factor was neglected and the quality of experimental conditions (laser, power measurement and camera) has improved since, an agreement of gain numbers from now and then within a factor of 2 to 3 was reasonable.

A spatial platform for breather research in nonlinear beam propagation was established and worked well, even when the system is relatively difficult with a few major approximations applied. Above all, the original cubic nonlinearity in the NLSE was boosted with a cascaded second-order nonlinearity. Second, we could not observe the nonlinear beam propagation inside the sample and a parameter scan was developed to characterize the nonlinear beam propagation. Finally, the results were time averaged over pulsed laser excitation. However, despite these approximations all important nonlinear beam properties could be characterized in good quality.

Acknowledgments. R. Schiek acknowledges the experimental support of F. Setzpfandt and T. Pertsch at the Institute of Applied Physics, Abbe Center of Photonics, Friedrich-Schiller-Universität Jena where the experiments have been performed. R. Schiek thanks F. Baronio at the Istituto Nazionale di Ottica CNR and Dipartimento di Ingegneria dell'Informazione, Università di Brescia for many fruitful discussions.

Disclosures. The author declares no conflicts of interest.

Data availability. Data underlying the results presented in this paper are not publicly available at the time but may be obtained from the author upon reasonable request.

References

1. J. W. Goodman, *Introduction to Fourier Optics* (McGraw-Hill, 1968).
2. V. E. Zakharov and L. A. Ostrovsky, "Modulation instability: The beginning," Phys. D **238**(5), 540–548 (2009).
3. P. Béjot, B. Kibler, E. Hertz, B. Lavorel, and O. Faucher, "General approach to spatiotemporal modulational instability processes," Phys. Rev. A **83**(1), 013830 (2011).
4. K. Tai, A. Tomita, J. L. Jewell, and A. Hasegawa, "Generation of subpicosecond solitonlike pulses at 0.3 THz repetition rate by induced modulational instability," Appl. Phys. Lett. **49**(5), 236–238 (1986).
5. R. Schiek, H. Fang, R. Malendevich, and G. I. Stegeman, "Measurement of Modulational Instability Gain of Second-Order Nonlinear Optical Eigenmodes in a One-Dimensional System," Phys. Rev. Lett. **86**(20), 4528–4531 (2001).
6. N. Akhmediev and V. I. Korneev, "Modulation instability and periodic solutions of the nonlinear Schrödinger equation," Theor. Math. Phys. **69**(2), 1089–1093 (1986).
7. O. Kimmoun, H. C. Hsu, H. Branger, M. S. Li, Y. Y. Chen, C. Kharif, M. Onorato, E. J. R. Kelleher, B. Kibler, N. Akhmediev, and A. Chabchoub, "Modulation Instability and Phase-Shifted Fermi-Pasta-Ulam Recurrence," Sci. Rep. **6**(1), 28516 (2016).
8. N. Akhmediev, J. M. Soto-Crespo, and A. Ankiewicz, "Extreme waves that appear from nowhere: On the nature of rogue waves," Phys. Lett. A **373**(25), 2137–2145 (2009).
9. M. Erkintalo, K. Hammani, B. Kibler, C. Finot, N. Akhmediev, J. M. Dudley, and G. Genty, "Higher-Order Modulation Instability in Nonlinear Fiber Optics," Phys. Rev. Lett. **107**(25), 253901 (2011).
10. B. Kibler, J. Fatome, C. Finot, G. Millot, F. Dias, G. Genty, N. Akhmediev, and J. M. Dudley, "The Peregrine soliton in nonlinear fibre optics," Nat. Phys. **6**(10), 790–795 (2010).
11. K. Hammani, B. Kibler, C. Finot, P. Morin, J. Fatome, J. M. Dudley, and G. Millot, "Peregrine soliton generation and breakup in standard telecommunications fiber," Opt. Lett. **36**(2), 112–114 (2011).
12. A. Mussot, C. Naveau, M. Conforti, A. Kudlinski, F. Copie, P. Szriftgiser, and S. Trillo, "Fibre multi-wave mixing combs reveal the broken symmetry of Fermi-Pasta-Ulam recurrence," Nat. Photonics **12**(5), 303–308 (2018).
13. A. Chabchoub, N. P. Hoffmann, and N. Akhmediev, "Rogue Wave Observation in a Water Wave Tank," Phys. Rev. Lett. **106**(20), 204502 (2011).
14. C. Cambournac, H. Maillotte, E. Lantz, J. M. Dudley, and M. Chauvet, "Spatiotemporal behavior of periodic arrays of spatial solitons in a planar waveguide with relaxing Kerr nonlinearity," J. Opt. Soc. Am. B **19**(3), 574–585 (2002).

Optics EXPRESS

15. D. Pierangeli, M. Flammini, L. Zhang, G. Marcucci, A. J. Agranat, P. G. Grinevich, P. M. Santini, C. Conti, and E. DelRe, "Observation of Fermi-Pasta-Ulam-Tsingou Recurrence and Its Exact Dynamics," Phys. Rev. X **8**(4), 041017 (2018).
16. R. Schiek and F. Baronio, "Spatial Akhmediev breathers and modulation instability growth-decay cycles in a quadratic optical medium," Phys. Rev. Res. **1**(3), 032036 (2019).
17. C. Naveau, P. Szriftgiser, A. Kudlinski, M. Conforti, S. Trillo, and A. Mussot, "Full-field characterization of breather dynamics over the whole length of an optical fiber," Opt. Lett. **44**(4), 763–766 (2019).
18. B. Frisquet, A. Chabchoub, J. Fatome, C. Finot, B. Kibler, and G. Millot, "Two-stage linear-nonlinear shaping of an optical frequency comb as rogue nonlinear-Schrödinger-equation-solution generator," Phys. Rev. A **89**(2), 023821 (2014).
19. B. Frisquet, B. Kibler, and G. Millot, "Collision of Akhmediev Breathers in Nonlinear Fiber Optics," Phys. Rev. X **3**(4), 041032 (2013).
20. B. Kibler, A. Chabchoub, A. N. Gelash, N. Akhmediev, and V. E. Zakharov, "Superregular Breathers in Optics and Hydrodynamics: Omnipresent Modulation Instability beyond Simple Periodicity," Phys. Rev. X **5**(4), 041026 (2015).
21. G. Xu, A. Gelash, A. Chabchoub, V. Zakharov, and B. Kibler, "Breather Wave Molecules," Phys. Rev. Lett. **122**(8), 084101 (2019).
22. G. Xu, K. Hammani, A. Chabchoub, J. M. Dudley, B. Kibler, and C. Finot, "Phase evolution of Peregrine-like breathers in optics and hydrodynamics," Phys. Rev. E **99**(1), 012207 (2019).
23. A. E. Kraych, D. Agafontsev, S. Randoux, and P. Suret, "Statistical Properties of the Nonlinear Stage of Modulation Instability in Fiber Optics," Phys. Rev. Lett. **123**(9), 093902 (2019).
24. S. Boscolo and C. Finot, *Shaping Light in Nonlinear Optical Fibers* (John Wiley& Sons, 2017), Chap. 10.
25. A. Fratalocchi, G. Assanto, K. A. Brzdakiewicz, and M. A. Karpierz, "Discrete propagation and spatial solitons in nematic liquid crystals," Opt. Lett. **29**(13), 1530–1532 (2004).
26. G. Van Simaeys, Ph. Emplit, and M. Haelterman, "Experimental Demonstration of the Fermi-Pasta-Ulam Recurrence in a Modulationally Unstable Optical Wave," Phys. Rev. Lett. **87**(3), 033902 (2001).
27. M. Erkintalo, G. Genty, B. Wetzel, and J. M. Dudley, "Akhmediev breather evolution in optical fiber for realistic initial conditions," Phys. Lett. A **375**(19), 2029–2034 (2011).
28. Y. Zhang, M. R. Belić, H. Zheng, H. Chen, C. Li, J. Song, and Y. Zhang, "Nonlinear Talbot effect of rogue waves," Phys. Rev. E **89**(3), 032902 (2014).
29. M. Conforti, A. Mussot, A. Kudlinski, S. Trillo, and N. Akhmediev, "Doubly periodic solutions of the focusing nonlinear Schrödunger equation: Recurrence, period doubling, and amplification outside the conventional modulation-instability band," Phys. Rev. A **101**(2), 023843 (2020).
30. N. Akhmediev, V. M. Eleonskii, and N. E. Kulagin, "Exact first-order solutions of the nonlinear Schrödinger equation," Theor. Math. Phys. **72**(2), 809–818 (1987).
31. J. M. Soto-Crespo, N. Devine, and N. Akhmediev, "Adiabatic transformation of continuous waves into trains of pulses," Phys. Rev. A **96**(2), 023825 (2017).
32. P. G. Grinevich and P. M. Santini, "The exact rogue wave recurrence in the NLS periodic setting via matched asymptotic expansions, for 1 and 2 unstable modes," Phys. Lett. A **382**(14), 973–979 (2018).
33. M. Crabb and N. Akhmediev, "Doubly periodic solutions of the class-I infinitely extended nonlinear Schrödinger equation," Phys. Rev. E **99**(5), 052217 (2019).
34. J. U. Kang, G. I. Stegeman, A. Villeneuve, and J. S. Aitchison, "AlGaAs below half bandgap: a laboratory for spatial soliton physics," Pure Appl. Opt. **5**(5), 583–594 (1996).
35. W. Krolikowski, B. Luther-Davies, and C. Denz, "Photorefractive Solitons," IEEE J. Quantum Electron. **39**(1), 3–12 (2003).
36. R. Schiek, "Nonlinear refraction caused by cascaded second-order nonlinearity in optical waveguide structures," J. Opt. Soc. Am. B **10**(10), 1848–1855 (1993).
37. R. Schiek, Y. Baek, and G. I. Stegeman, "One-dimensional spatial solitary waves due to cascaded second-order nonlinearities in planar waveguides," Phys. Rev. E **53**(1), 1138–1141 (1996).
38. R. Schiek, Y. Baek, and G. I. Stegeman, "Second-harmonic generation and cascaded nonlinearity in titanium-indiffused lithium niobate channel waveguides," J. Opt. Soc. Am. B **15**(8), 2255–2268 (1998).
39. A. V. Buryak, Y. S. Kivshar, and S. Trillo, "Optical solitons supported by competing nonlinearities," Opt. Lett. **20**(19), 1961–1963 (1995).
40. K. Hammani, B. Wetzel, B. Kibler, J. Fatome, C. Finot, G. Millot, N. Akhmediev, and J. M. Dudley, "Spectral dynamics of modulation instability described using Akhmediev breather theory," Opt. Lett. **36**(11), 2140–2142 (2011).

212.201.131.5 {ts '2022-03-15 15:48:36'}